energies

MDPI

Article

Exploring the Potential of Kite-Based Wind Power Generation: An Emulation-Based Approach

Roystan Vijay Castelino [1], Pankaj Kumar [1], Yashwant Kashyap [1,*], Anabalagan Karthikeyan [1], Manjunatha Sharma K. [1], Debabrata Karmakar [2] and Panagiotis Kosmopoulos [3,*]

1 Department of Electrical & Electronics Engineering, National Institute of Technology Karnataka, Surathkal, Mangalore 575025, India; roycas3@gmail.com (R.V.C.); pankajkumar.217ee006@nitk.edu.in (P.K.); jakarthik@nitk.edu.in (A.K.); kms@nitk.edu.in (M.S.K.)

2 Department of Water Resources and Ocean Engineering, National Institute of Technology Karnataka, Surathkal, Mangalore 575025, India; dkarmakar@nitk.edu.in

3 Institute for Environmental Research and Sustainable Development, National Observatory of Athens (IERSD/NOA), 15236 Athens, Greece

* Correspondence: yashwant.kashyap@nitk.edu.in (Y.K.); pkosmo@noa.gr (P.K.)

Abstract: A Kite-based Airborne Wind Energy Conversion System (KAWECS) works by harnessing the kinetic energy from the wind and converting it into electric power. The study of the dynamics of KAWECS is fundamental in researching and developing a commercial-scale KAWECS. Testing an actual KAWECS in a location with suitable wind conditions is only sometimes a trusted method for conducting research. A KAWECS emulator was developed based on a Permanent Magnet Synchronous Machine (PMSM) drive coupled with a generator to mimic the kite's behaviour in wind conditions. Using MATLAB-SIMULINK, three different power ratings of 1 kW, 10 kW, and 100 kW systems were designed with a kite surface area of 2.5 m^2, 14 m^2, and 60 m^2, respectively. The reel-out speed of the tether, tether force, traction power, drum speed, and drum torque were analysed for a wind speed range of 2 m/s to 12.25 m/s. The satellite wind speed data at 10 m and 50 m above ground with field data of the kite's figure-of-eight trajectories were used to emulate the kite's characteristics. The results of this study will promote the use of KAWECS, which can provide reliable and seamless energy flow, enriching wind energy exploitation under various installation environments.

Keywords: high altitude wind power; kite-based airborne wind energy conversion system; kite emulator; PMSM; renewable energy

check for updates

Citation: Castelino, R.V.; Kumar, P.; Kashyap, Y.; Karthikeyan, A.; Sharma K., M.; Karmakar, D.; Kosmopoulos, P. Exploring the Potential of Kite-Based Wind Power Generation: An Emulation-Based Approach. *Energies* **2023**, *16*, 5213. https://doi.org/10.3390/en16135213

Academic Editor: Davide Astolfi

Received: 27 May 2023
Revised: 16 June 2023
Accepted: 5 July 2023
Published: 6 July 2023

1. Introduction

Renewable energy generation and implementation are crucial for minimising the impact of fossil fuel emissions on the environment. Renewable technology development comes with challenges that restrict endorsement. Wind energy is one option for decarbonising the energy system. Wind turbines were used to generate electricity in the 1880s [1]. Among all renewable energies, wind power is one of the most rapidly growing industries in the world because it has many benefits, such as a high capacity factor, low maintenance costs, and low carbon emissions. By 2030, wind power alone will provide 20% of the world's energy needs [2]. Various wind turbines have been designed for this purpose, each with unique core subsystems for converting wind into electricity [3,4].

An Airborne Wind Energy System (AWES) is a high-altitude wind energy conversion system that uses one or more kites, gliders, or horizontal flying turbines that are tethered to a ground station to produce energy [5]. The AWES was designed to improve existing technologies by focusing on catching winds at high altitudes and turning them into electricity [6]. Loyd demonstrated that a tethered wing the size of a C-5A aircraft could generate 6.7 MW of electrical power with a wind speed of 10 m/s. The generated power is three times more than the conventional wind turbine-generated power [7]. Since then, most of the prototypes for airborne wind energy systems are still in the early stages of development [8]. AWES technology's improved availability, stability, and reduced prices make it economically viable [9]. The autonomous takeoff and flying of a tethered aircraft verify the technological viability of the proposed takeoff approach, allowing for deploying this AWES technology in a small area at a low cost [10]. An economic analysis at an existing site indicated that AWES costs less to transport and assemble and has a larger potential capacity, resulting in more significant economic advantages [11]. Consequently, a little increase in the operating altitude of the wind energy system can result in a significant rise in the produced power. AWES can access winds at heights between 0.1 km and 2 km [8,12].

AWE systems may obtain ideal wind speeds by adjusting their operational height by modifying the elevation angle and sometimes tether length, unlike traditional wind turbines [13]. This development allows for bigger wind turbines to be placed at higher altitudes, where the wind is predicted to be stronger and more constant due to the high altitude. The amount of extractable wind energy rises by the order of the wind speed cube [14]. A significant amount of research is being conducted at the moment to enhance kite-direction control by implementing various control strategies, including predictive control [15–18]. The various choices of airfoils for extracting electricity from such a system are proposed in the literature [19–22]. In this paper, the focus is on a pumping mode Kite-based Airborne Wind Energy Conversion System (KAWECS). The KAWECS is a promising method for capturing the power from winds at high altitudes. A KAWEC system's simplified structure is depicted in Figure 1.

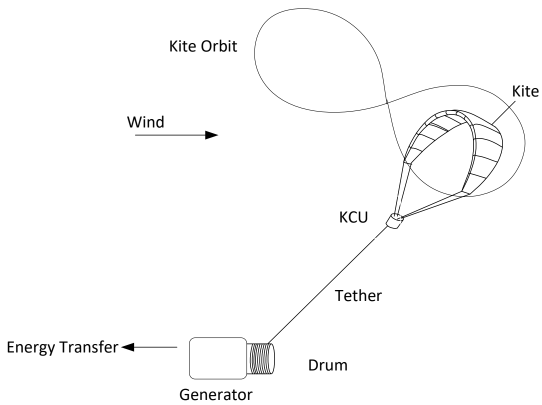

Figure 1. Technique for producing electricity by kite flight: the kite follows a figure-of-eight path, which pulls the tether looped on the drum and turns the generator to provide electric power.

The ground station consists of a drum coupled to a generator for electrical power generation. A complete operation cycle consists of two operation phases: the traction and recovery phases. During the traction phase, the kite extracts the kinetic energy from the wind by crosswind manoeuvres and the aerodynamic force is transferred to the ground through the tether. The tether is wound on a spool connected to the shaft of the generator and is rotated by the pull of the tether. Once the wing has reached a predetermined maximum tether length, the AWES enters the recovery phase. This phase uses energy to restore the tether to its original length. The generator is typically used as a motor during this stage in current prototype systems [23]. The kite is controlled to fly with a high crosswind speed to extract energy from high altitudes. As a result, a powerful pulling force is created, turning the generator to produce energy.

In the literature, most of the KAWECS use a Permanent-Magnet Synchronous Machine (PMSM) as an electric power generator [24]. As the KAWECS operates in pumping cycles, the speed of the generator and the power output are variable and highly dependent on the wind speed. An appropriate wind condition or field location for researching an actual KAWECS is very challenging [18]. Therefore, designing airborne wind energy system dynamics and airborne wind energy turbine emulation is convenient. Although there are a lot of Conventional Wind Turbine (CWT) emulations based on PMSM drives [25–27], there is limited literature on the implementation of KAWECS-based emulators. The simulation of power generation using PMSM is explained in the literature but they lack in the discussion related to drum-side mechanical power production [17,28,29], which is crucial in KAWECS. In addition, the study of scaling the power levels using a PMSM-based approach is missing in the literature [30,31]. The primary motivation for this research work is the development of commercial-scale KAWECS. The emulated power's accuracy depends on the kite's modelling and the data used for the emulation [17]. Another aspect of the system is scalability, which is not discussed in the literature [17,32,33]. We propose a KAWECS emulator based on FOC-controlled PMSM with experimental kite data and discuss the system's potential with 1 kW, 10 kW, and 100 kW systems. The KAWECS is also compared with CWT to evaluate the energy production capabilities of the KAWECS.

Figure 2 shows the proposed block diagram of KAWECS, which consists of five parts. The first part is the kite system, which gives the output in the form of torque and reel-out speed, and it translates into mechanical power; this automated power control in the kite emulator system is shown in the second block, which consists of a controller, a power converter, and permanent magnet synchronous motor (PMSM), which, in combination, is known as a drum. The drum is mechanically coupled with a PMSG (permanent magnet synchronous generator) that transforms mechanical energy into electrical energy. The main contributions and novelty of this proposed research work are as follows:

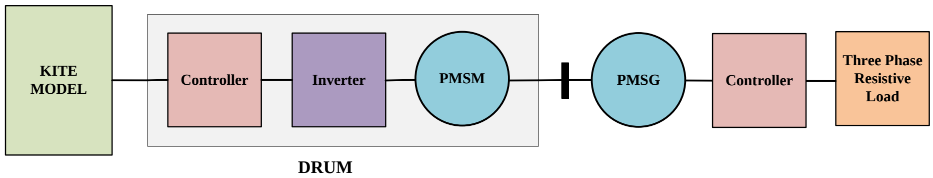

Figure 2. Block diagram of a kite power generation system.

- The study analysed the scalability of the KAWECS using PMSM and key results are discussed in the paper;
- The dynamic behaviour of a kite-based wind power generation. The effects of wind speed in terms of reel-out speed, tether force, traction power, drum speed, and drum torque are described;
- The design, simulation, and implementation of an airborne wind energy turbine emulator system built using PMSM is outlined;
- The KAWECS emulator was tested with the experimental data from the field tests and the behaviour of the system is described.

The paper is organised as follows: The mathematical formulations of the kite model, PMSM model, simulation model, the emulator model, and the comparison with the conventional wind turbine is described in Section 2. The simulation results and the discussions are presented in Section 3, which describe the dynamic behaviour of the kite; further, we present no-load, on-load, and field test data analyses with experimental ground data simulation results. Section 4 concludes the research outcomes and explains future works.

2. KAWECS Emulator Modelling

2.1. Kite Dynamics

The wind reference frame serves as the initial point of reference for the analysis, as shown in Figure 3. Its origin, 'O', coincides with the location where the rope exits the ground station, and both its Z-axis and X-axes are oriented in the direction of the wind. We employ a spherical coordinate system (r, θ, ϕ) and the methods described in references [34–36] to define its position K and velocity $u_a \in \Re$ [m/s]. The radial distance $r \in \Re$ [m], polar angle $\theta \in \Re$ [rad], and azimuth angle $\phi \in \Re$ [rad] are used to represent the position. The course angle $\chi \in \Re$ [rad] indicates the direction of flight in the local tangential plane. Figure 3a shows the geometrically similar velocity and force diagrams, where u_a and F_a are decomposed in the vector plane. When assuming a straight tether and a minimal mass effect, $u_{a,r}$ aligns with F_a. In Figure 3b, the kite velocity u_k is decomposed in radial direction $u_{k,r}$ and tangential direction $u_{k,t}$. The apparent wind velocity u_a is defined as the difference between the wind velocity u_w and the velocity of the kite u_k. The course angle χ is measured in the tangential plane defined in the wind framework for reference X, Y, and Z axes.

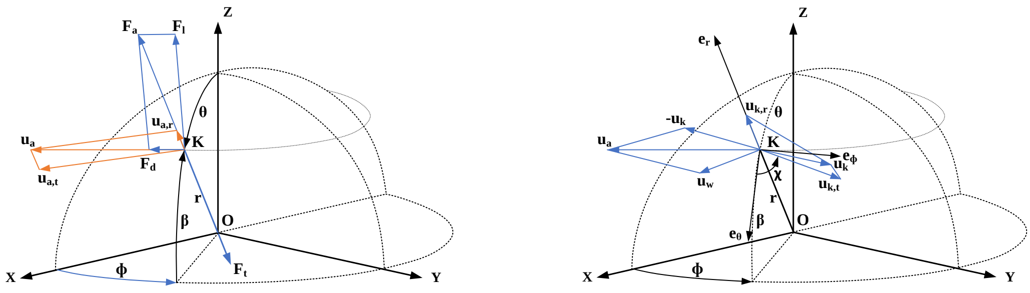

(**a**) (**b**)

Figure 3. Spherical coordinate and geometrically decomposition of the kite system: (**a**) shows that the force and speed representations are geometrically comparable. (**b**) shows the decomposing kite velocity into radial and tangential components.

The apparent wind speed characterises the flow rate in relation to the kite velocity [34].

$$u_a = u_w - u_k \tag{1}$$

We can also write the apparent wind speed in spherical coordinates as shown below.

$$u_a = \begin{bmatrix} \sin\theta\cos\phi \\ \cos\theta\sin\phi \\ -\sin\phi \end{bmatrix} u_w - \begin{bmatrix} 1 \\ 0 \\ 0 \end{bmatrix} u_{k,r} - \begin{bmatrix} 0 \\ \cos\chi \\ -\sin\chi \end{bmatrix} u_{k,t} \tag{2}$$

where the kite's radial and tangential contributions to its speed are denoted by $u_{k,r}$ and $u_{k,t}$, respectively.

The straight tether suggests that the reeling speed and radial kite speed are the same, and this assumption implies that the tether mass is neglected to simplify the simulation approach.

$$u_{k,r} = u_{k,t} \tag{3}$$

The reeling factor can be written as

$$p = \frac{u_{k,r}}{u_w} \tag{4}$$

The tangential speed factor can be written as

$$q = \frac{u_{k,t}}{u_w} \tag{5}$$

The second equation may be written as

$$u_a = \begin{bmatrix} \sin\theta\cos\phi - p \\ \cos\theta\sin\phi - q\cos\chi \\ -\sin\phi - q\sin\chi \end{bmatrix} u_w \tag{6}$$

The steering system controls the course angle χ, the ground station controls the reeling factor p, and the force equilibrium determines the dependent variable, i.e., the tangential speed factor q. The kite flies in figure-of-eight crosswind trajectories and the aerodynamic force of the kite varies throughout the flight. The figure-of-eight trajectory data were taken from field tests to compute the aerodynamic forces of the kite, which is discussed in Section 3.4.

The components of the airborne wind energy system's integral aerodynamic force can be separated into the lift and drag forces:

$$\vec{F_a} = \vec{F_L} + \vec{F_D} \tag{7}$$

The lift force and drag force are written as

$$\vec{F_L} = \frac{1}{2}\rho C_L u_a^2 A \tag{8}$$

and

$$\vec{F_D} = \frac{1}{2}\rho C_D u_a^2 A \tag{9}$$

The kite projected surface area $A \in \Re$ [m^2] , the apparent wind speed $u_a \in \Re$ [m/s], the air density $\rho \in \Re$ [kg/m^3], and the lift and drag coefficients are denoted C_L and C_D, respectively.

The aerodynamic force is represented as

$$\vec{F_a} = \frac{1}{2}\rho C_R u_a^2 A \tag{10}$$

where

$$C_R = \sqrt{C_D^2 + C_L^2} \tag{11}$$

Assume the aerodynamic force $F_a \in \Re$ [N] is balanced by the tether force $F_t \in \Re$ [N] shown in Figure 3, and is represented as

$$\vec{F_t} = -\vec{F_a} \tag{12}$$

The reel-out Speed $u_r \in \Re$ [m/s] is calculated using the wind speed $v_w \in \Re$ [m/s] and lift force $F_L \in \Re$ [N] as described in Reference [37].

$$u_r = v_w \sin\theta \cos\phi - \sqrt{-h^2 - g^2 + \frac{2F_L}{C_L A \rho}} \tag{13}$$

$$h = u_{k,t} \sin\chi + v_w \sin\phi, \qquad g = u_{k,t} \cos\chi - v_w \cos\phi \cos\theta$$

According to Loyd's calculations, the maximum amount of mechanical power can be generated at a specific reel-out speed u_r. This is provided by

$$u_r = \frac{1}{3} \cdot v_w \tag{14}$$

The drum speed relating to the tether reel-out speed is given by

$$u_r = r \cdot \omega_d \tag{15}$$

where u_t is the reel-out speed of the tether, ω_d is the angular velocity of the drum, and r is the drum radius. Figure 4 shows the interaction between the kite tether and the drum. The drum torque $(T_d) \in \Re$ [Nm] is equal to the multiplication of the drum radius and the tether force:

$$T_d = F_t \cdot r = F_t \cdot \frac{D}{2} \tag{16}$$

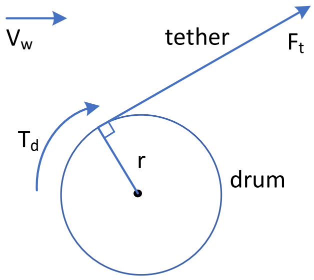

Figure 4. Interaction of drum and the kite tether.

From Equation (14), by knowing the wind speed (m/s), we can obtain the reel-out speed of the tether (m/s). With the additional input of the diameter of the drum, the optimum speed of the drum (RPM) can be estimated using the following equation:

$$N_d = \frac{u_r}{2\pi r} \cdot 60 = \frac{u_r}{\pi D} \cdot 60 \tag{17}$$

where D is drum diameter $\in \Re$ [m], and N_d is the drum speed $\in \Re$ [rpm].

The drum power (P_d) $\in \Re$ [W] of the kite is calculated by multiplying the drum torque by the drum speed in the following formula:

$$P_d = T_d \cdot \omega_d \tag{18}$$

where ω_d is the drum speed $\in \Re$ [rad/s].

2.2. PMSM Modelling

The equivalent electric model of PMSM shown in Figure 5, which comprises the stator phase resistance $R_s \in \Re$ [Ω], the synchronous inductance $Ls \in \Re$ [H], and EMF $Es \in \Re$ [V], can be employed to represent each machine's phase. Here, we consider the synchronous inductance (L_s) to be equal to the quadrature-axis inductance (L_q) and direct-axis inductance (L_d). The magnetic circuit is assumed to have linear properties (saturation neglected), a constant air gap, and the sinusoidal behaviour of a three-phase current.

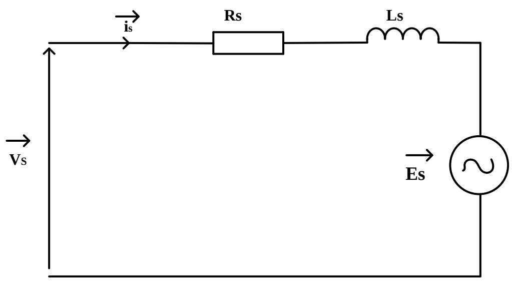

Figure 5. Equivalent electrical circuit of PMSM.

The variable vector presentation shows all three phases at the same time. It is shown in park coordinates (d, q) by [38]

$$v_{sq} = R_s i_{sq} + L_s \frac{di_{sq}}{dt} + \omega L_s i_{sd} + w\phi_{fsd} \tag{19}$$

$$v_{sd} = R_s i_{sd} + L_s \frac{di_{sd}}{dt} - \omega L_s i_{sq} \tag{20}$$

$$\phi_{sd} = L_s i_{sd} + \phi_{fsd} \tag{21}$$

$$\phi_{sq} = L_s i_{sq} \tag{22}$$

$$T_e = p\phi_{fsd} i_{sq} \tag{23}$$

where the voltage at the stator is represented by the vector $\vec{v_s} = v_{sd} + j \cdot v_{sq}$, the current at the stator is represented by the vector $\vec{i_s} = i_{sd} + j \cdot i_{sq}$, the flux produced by PMSM is $\vec{\Phi_{fs}} = \phi_{fsd} + \phi_{fsq}$, ω is the electric pulsation, and p is the number of pole pairs.

The voltage source inverter circuit shown in Figure 6 has six toggle switches and operates from a supply voltage of V_{dc}. Depending on the use case, the AC voltage's frequency may be changed or held constant. Reference voltages are generated by the current regulators; these voltages are then inverted using the field-oriented control technique developed by Park and Clarke transformation. The sinusoidal pulse width modulation generator uses the reference voltage as input to generate switching pulses for the three-phase inverter. This dc input voltage is sent into the three-phase inverter, which, in turn, generates an ac output voltage that drives the motor [39].

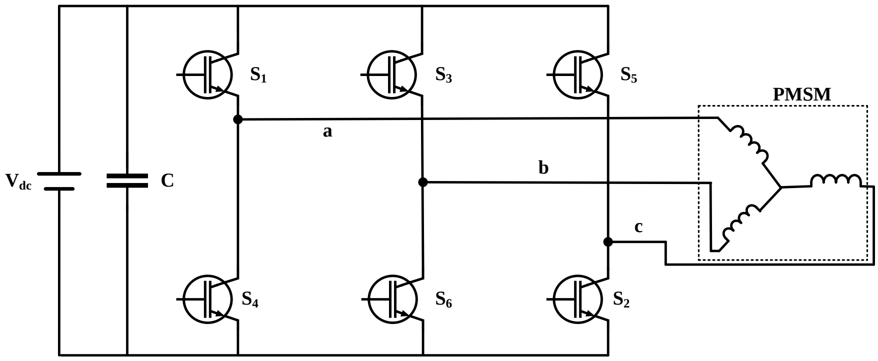

Figure 6. Kite (gear ratio and drum) conversion system using power converter with PMSM.

Park and Clarke transform is used to convert from three phases (*abc*) to two phases (*dq*), which is written as

$$v_{sq} = \frac{2}{3}\left[V_a \cos\theta + V_b \cos(\theta - \frac{2\pi}{3}) + V_c \cos(\theta + \frac{2\pi}{3})\right] \tag{24}$$

$$v_{sd} = -\frac{2}{3}\left[V_a \sin\theta + V_b \sin(\theta - \frac{2\pi}{3}) + V_c \sin(\theta + \frac{2\pi}{3})\right] \tag{25}$$

In addition, inverse Park and Clarke transform is used to convert from two phases (*dq*) to three phases (*abc*), which is written below.

$$V_a = V_q \cos\theta - V_d \sin\theta \tag{26}$$

$$V_b = V_q \cos(\theta - \frac{2\pi}{3}) - V_d \sin(\theta - \frac{2\pi}{3}) \tag{27}$$

$$V_c = V_q \cos(\theta + \frac{2\pi}{3}) - V_d \sin(\theta + \frac{2\pi}{3}) \tag{28}$$

The three-phase electrical output power of the generator is written below.

$$P_e = \sqrt{3} \cdot V_L \cdot I_L \cos\phi \tag{29}$$

where V_L and I_L are the generator voltage and current, respectively. $\cos\phi$ is the power factor. The kite power evaluated using Equation (18) and the generator output power evaluated using Equation (29) are equal.

2.3. Simulation Model

Figure 7 depicts the simulation of the reel-out speed, tether force, drum speed, and drum torque using the MATLAB SIMULINK environment. The parameters used for the kite were the same as those discussed in Section 2. The following two lift and drag force blocks were used to compute the lift and drag forces based on Equations (8) and (9), respectively. The resultant aerodynamic force based on Equation (10), which is equal to the tether force, was computed and displayed in the third block. The reel-out speed estimator shown in block four was estimated based on Equations (13) and (14), and the last block is a drum, which produces the drum torque and speed based on Equations (16) and (17), respectively.

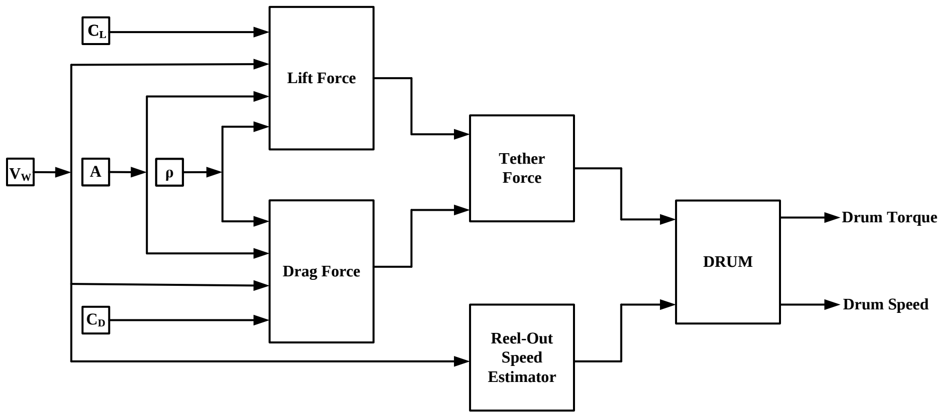

Figure 7. Wind speed to the kite force (torque and speed) conversion system in Matlab Simulink.

The drum speed $(\omega_d) \in \Re$ [rad/s] in terms of the tether force is shown below.

$$\omega_d = \frac{P_d}{F_t.(\frac{D}{2})} \tag{30}$$

where P_d is the drum power in watts, F_t is the tether force, and D is the drum diameter. This equation provides the relation between the tether force and drum speed.

Figure 8 shows the flow chart and gives an overall view of the methodology used in this investigation. The first block shows the collection of the wind data (A, C_L, C_D, ρ, and u_w) depicted in Table 1, which is the input parameter of the kite dynamic block. The dynamic kite block generates mechanical kite power using Equation (18). In the next stage, the dram dynamic estimates the torque and speed using Equations (16) and (17), respectively.

Table 1. The KAWECS emulator parameters of three different test cases.

Parameter	1 kW	10 kW	100 kW
Kite Area	2.5 m^2	14 m^2	60 m^2
Aerodynamic Coefficient, C_R	1.125	2.875	3.825
Wind Speed	2–12.25 m/s	2–12.25 m/s	2–12.25 m/s
Air Density	1.225 kg/m^3	1.225 kg/m^3	1.225 kg/m^3
Rated Voltage of Machines	415 V	415 V	415 V
Rated Speed of Machines	1500 rpm	1500 rpm	1500 rpm
Pole Pairs of Machines	4	4	4
Rated Current of Machines	1.5 A	14 A	135 A
Maximum Torque of Machines	6 Nm	65 Nm	630 Nm

The torque and speed of the PMSM motor is controlled using field-oriented control technique in the next phase. In the next step, a torque and speed sensor measures the motor's speed and torque and compares them to the reference speed and torque; if the two do not match, the control is returned to the controller, which fixes the error. In the next stage, PMSG converts mechanical power to electrical power. The output of the PMSG is connected to the controlled resistive load through a load controller.

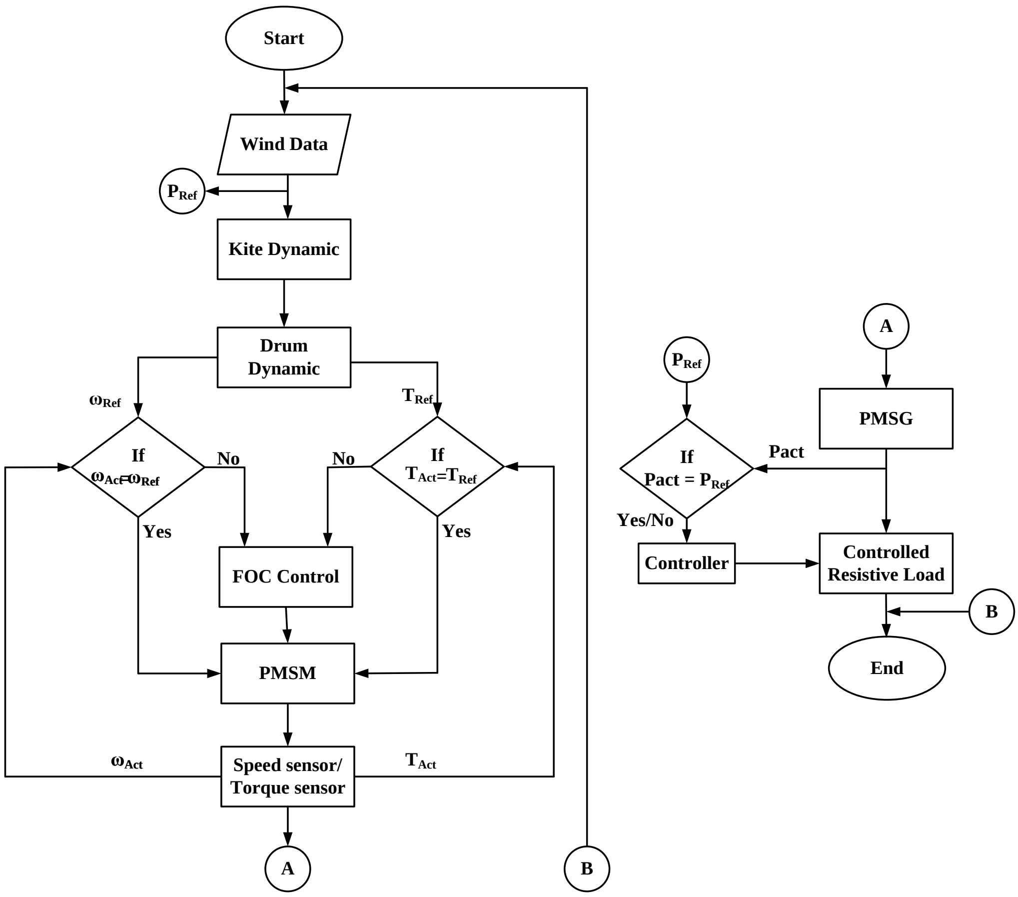

Figure 8. Flow chart of KAWECS emulator.

2.4. Emulator Model

The kite emulator consists of a combination of a kite model, a permanent magnet synchronous motor, a three-phase inverter (DC/AC converter), and controllers. PMSM is used to mimic the KAWECS characteristics. The PMSM is regulated by following the kite airborne wind turbine's torque command. The motor provides high-performance torque control using the field orientation control (FOC) method.

The developed PMSM-based KAWECS system's overall control mechanism is shown in Figure 9. The power inverter uses sinusoidal pulse width modulation (SPWM) to supply the motor with three-phase power. Using the rotor angle determined by a sensing element integrated into the PMSM, the PMSM's phase currents are mapped and measured relative to a rotational reference frame. Motor phase currents are regulated by keeping the d-axis current at zero and the q-axis current at a value high enough to issue the reference torque at all speeds below or equal to the rotor speed.

The generator, which is also a permanent magnet synchronous machine, is coupled to the emulator, and the load, which is a regulated resistive load, is managed by the load controller. In the outer loop for speed control, the reference speed (ω_{Ref}) value is compared with the actual speed (ω_{Act}) value and determines the error in the calculated speed. In the current feedback loop, the speed deviation is amplified proportionally and integrally before being denoted as the quadrature-axis current. The size and polarity of the reference current define the direction and magnitude of the torque produced by the PMSM. The torque generated by the synchronous permanent magnet motor now causes the rotational speed to approach the nominal value. Putting the reference of the direct-axis current controller at zero allows for independent control of the torque along the q-axis current.

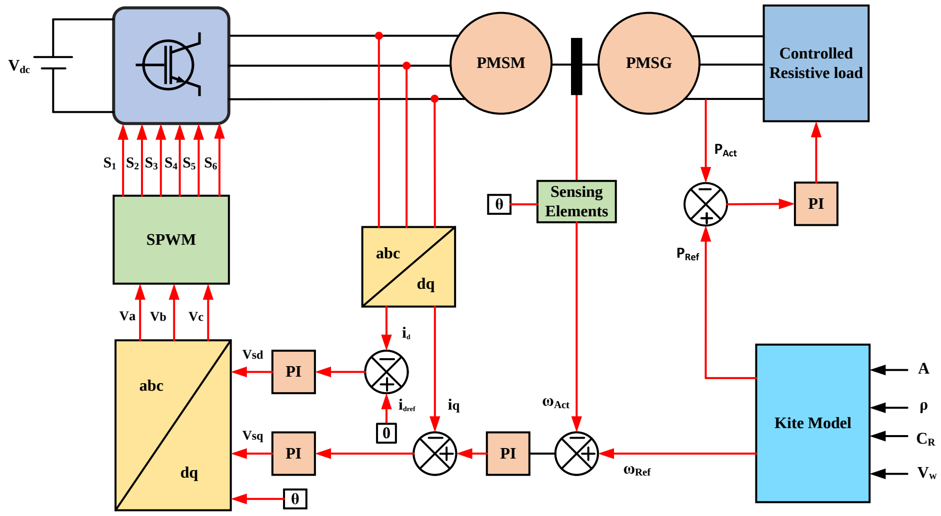

Figure 9. Control mechanism of proposed KAWECS emulator.

The speed controller loop is depicted in Figure 10; the error in measured speed is calculated by comparing the reference speed (ω_{Ref}) with the actual speed (ω_{Act}). The speed error is amplified proportionally and integrally before being sent into a current feedback loop, where it is known as the quadrature-axis current.

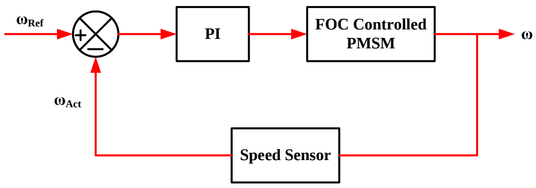

Figure 10. Motor speed controller loop.

Figure 11 shows the output electrical power control loop. The reference kite power (P_{Ref}) value is compared with the actual electrical output power of the PMSG (P_{Act}) value, which determines the error in the measured electrical power. Once the output power error has been amplified proportionally and integrally, it is sent to the power feedback loop, where it is known as the electrical load power.

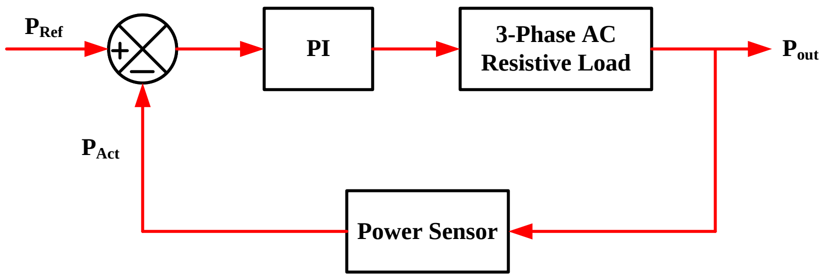

Figure 11. Load controller loop.

Table 1 represents the system parameters for the simulation of KAWECS, as shown in the table below.

2.5. Comparison with Conventional Wind Turbine

The commercialization of KAWECS mainly depends on its scalability and capacity factor. The KAWECS and the CWTs both generate energy from the wind, but they differ in their design and operation. A distinct feature of KAWECS is that it can generate electricity at higher altitudes, where the wind is strong and consistent. This can make the KAWECS more efficient than the CWTs, which are limited by the height of the blades. The mechanical power (P_m) developed by a CWT is given by [40]

$$P_m = \frac{1}{2}\rho\pi R^2 C_p(\lambda, \beta) v_w^3 \tag{31}$$

where ρ is the air density, R is the radius of the area swept by the turbine, and C_p is the power coefficient, which is the ratio of mechanical power to the power in the wind. C_p is a function of the Tip Speed Ratio (TSR) denoted by λ and the pitch angle of the turbine blade β. The λ is calculated as the tip speed divided by the wind speed.

The mechanical torque T_m developed by the CWT is given by [41]

$$T_m = \frac{1}{2}\frac{\rho\pi R^3 C_p(\lambda, \beta) v_w^2}{\lambda} \tag{32}$$

The value of C_p varies nonlinearly with λ and β, and varies with respect to the turbine design. From Equations (31) and (32), we can infer that, by knowing the values of v_w, λ, and β, we can evaluate the mechanical torque developed by the turbine. As the KAWECS operates in pumping mode, the maximum power generated in a cycle of operation P_{cyl}, which includes the power generated during tether reel-out P_{rout} and the power spent during the reel-in P_{rin} of the kite, is given by

$$P_{cyl} = P_{rout} - P_{rin} \tag{33}$$

Table 2 shows the data used for the comparison of KAWECS with CWT, which is taken from the literature [11]. From Table 2, we can observe that a KAWECS with a projected area of 270.9 m^2 attains the rated power at 7.3 m/s, which is much lesser than the CWT, making it suitable for low wind profile regions. The maximum power from the KAWECS is limited to 1322 kW, which is due to the power consumed in the reeling-in of the kite. The capacity factor of the KAWECS is 45.59% as compared to 31.36% of CWT, indicating a 45% increased average power production from a KAWECS plant as compared to a CWT plant.

Table 2. Specifications of KAWECS and CWT [11].

Parameters	**KAWECS**	**CWT**
Nominal Power (P_{nom})	2 MW	2 MW
Specifications	Wing span = 36.8 m Projected Area = 270.9 m^2 Tether diameter = 3 cm Reel-out length = 230 m Max tension = 56.09 ton	Hub height = 78 m Blade length = 43 m Area swept = 5808.0 m^2 TSR = 6.7 C_p = 0.43
Rated Wind Speed at P_{nom}	7.3 m/s	9.8 m/s
Max Power	$P_{cyl,max}$ = 1322 kW P_{rout} = 2 MW P_{rin} = 678 kW	P_{max} = 2 MW
Average Power (P_{avg})	911 kW	627 kW
Capacity Factor (C_F)	45.59%	31.36%

3. Simulation Results and Discussion

This section discusses the results of KAWECS under no load and with an AC resistive load conditions. The KAWECS emulator presented in the block diagram (Figure 9) was implemented and simulated in MATLAB/Simulink, and the results are shown considering a variable wind speed from 2 m/s to 12.25 m/s. The plots of the kite dynamics, power converter output, PMSM output, and the PMSG output parameters are discussed in detail.

3.1. No-Load Test

Figure 12 shows the simulation results of the KAWECS emulator under no-load condition using the data shown in Table 1. Figure 12a depicts the motor speed at no load, which varies between 253.54 rpm to 1500 rpm, and the minimum and maximum speeds of the motor, which are the same as the motor's reference speed.

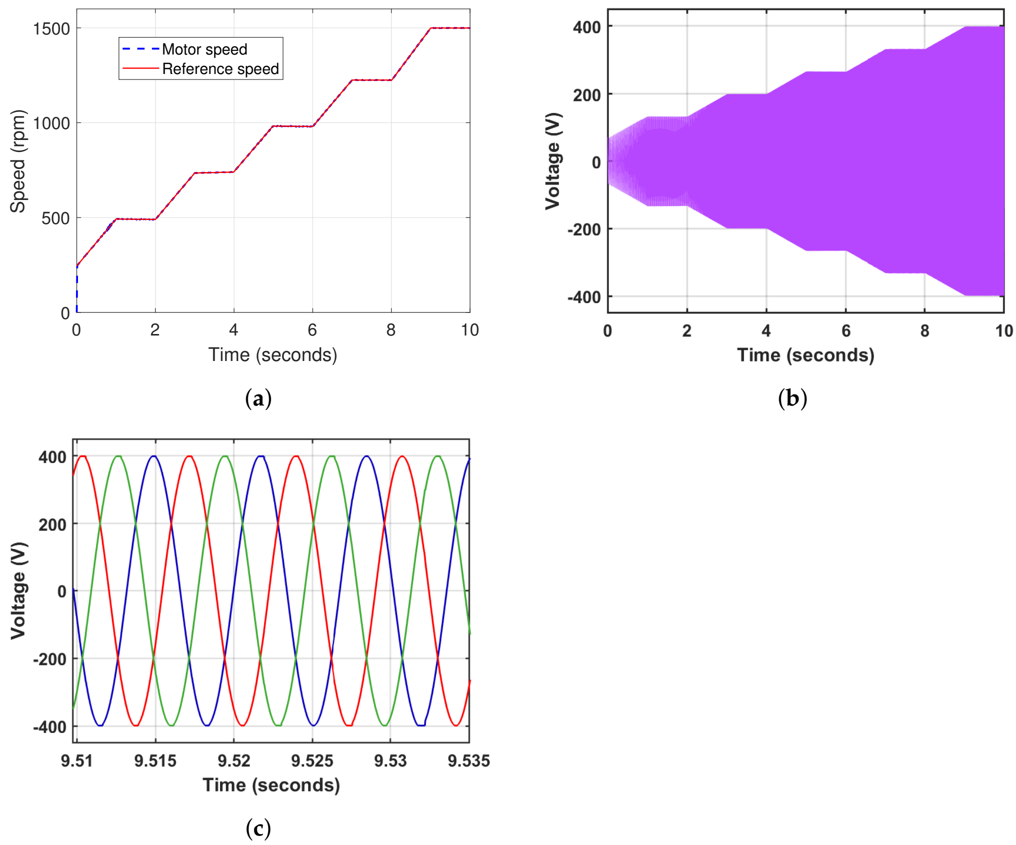

Figure 12. No-load analysis at generator terminal: (**a**) no-load speed of coupled machines; (**b**) no-load generator voltage; and (**c**) no-load generator voltage (zoomed) denoting 3-phase voltages.

Figure 12b represents the generator voltage, which changes from 68 V to 133 V in 0 to 2 s and 334 V to 400 V in a period of 8 to 10 s at the corresponding wind speed. Figure 12c is a zoomed-in section of Figure 12b, which shows the three-phase voltage of the generator. From the no-load analysis, the FOC control of the PMSM was validated, which follows the reference speed from the kite model.

3.2. On-Load Test

Figure 13 shows the KAWECS simulation results with the AC resistive load analysis at the PMSG terminal using the parameters shown in Table 1. Figure 13a depicts the variation in the motor current, which changes according to the load torque. The motor current varies from 2.64 A to 33.45 A, which is the minimum and maximum current of the motor from period 0 to 10 s at wind speeds of 2 m/s to 12.25 m/s, respectively. Figure 13b shows the enlarged form of the motor current, which is depicted in Figure 13a. Figure 13c represents the motor input power, which is the motor's electrical power. It varies from 33 W to 6950 W with a time variation from 0 to 10 s at wind speeds of 2 m/s to 12.25 m/s, respectively.

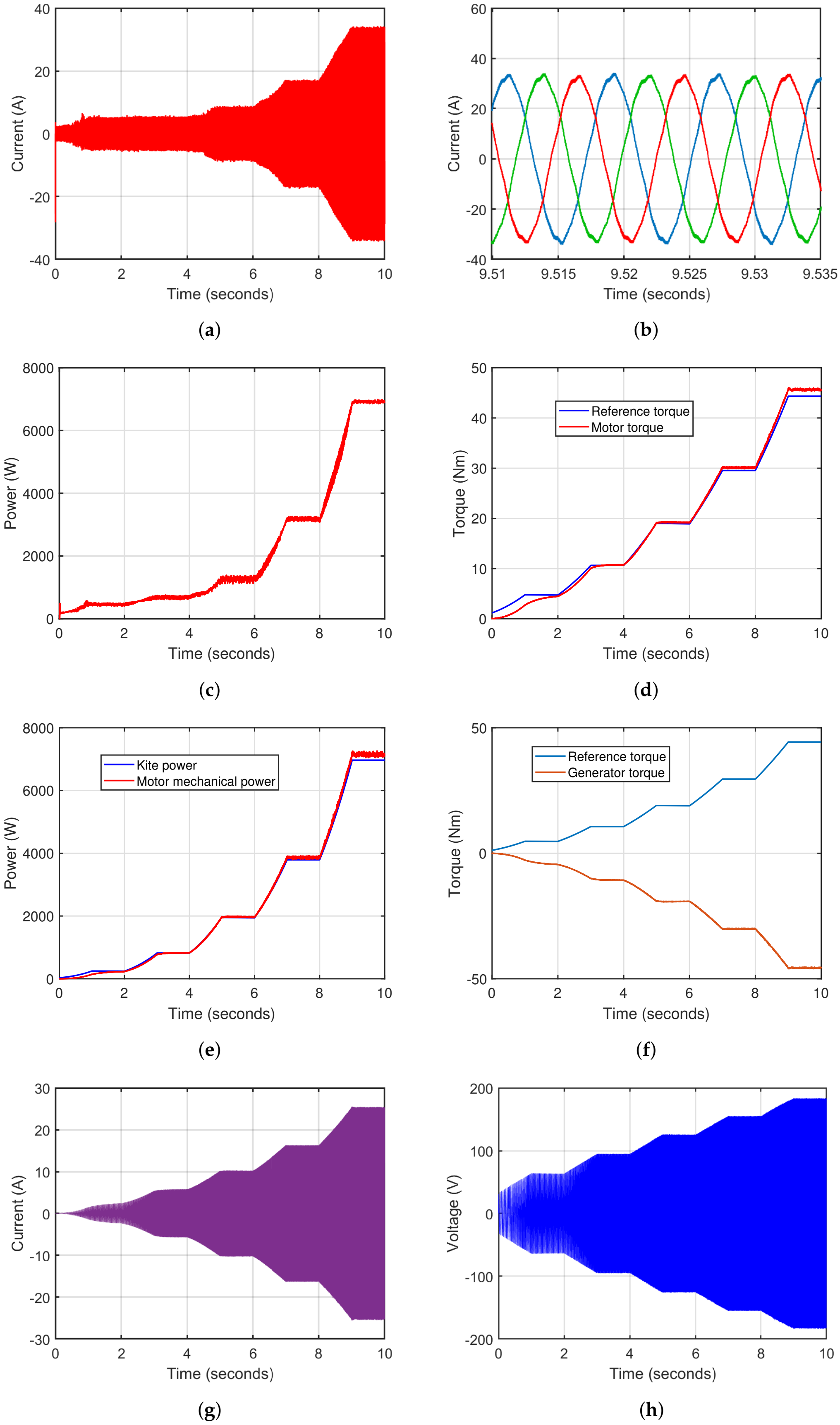

Figure 13. *Cont.*

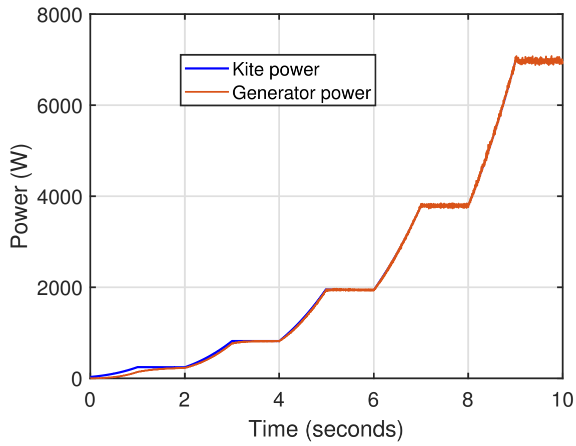

(**i**)

Figure 13. Simulation results: (**a**) motor current; (**b**) motor current (zoomed-in view); (**c**) electrical power of the motor; (**d**) coupling torque; (**e**) coupling power; (**f**) generator torque; (**g**) generator AC current; (**h**) generator AC voltage; and (**i**) generator output power.

Figure 13d shows the torque variation, with the blue waveform representing the kite torque and the red waveform representing the motor torque. It varies from a minimum torque of 1.27 Nm at a 2 m/s wind speed and a maximum torque of 45 Nm at 12.25 m/s for the period of 0 to 10 s, which follows the motor reference torque. The motor and generator coupling power is depicted in Figure 13e. It changes from 33 W to 7000 W, with a corresponding wind speed of 2 m/s to 12.25 m/s, which precisely follows the reference power of the kite. Figure 13f shows the generator torque, which is the negative of the motor torque. It changes from −1.27 Nm to −45 Nm at wind speed varying from 2 m/s to 12.25 m/s. Figure 13g shows the generator's current, which changes from 0 A to 27 A and the corresponding wind speeds from 2 m/s to 12.25 m/s, respectively. Figure 13h shows the generator's AC voltage, which changes from 68 V to 198 V, and the corresponding wind speed from 2 m/s to 12.25 m/s, respectively. Figure 13i depicts the generator's electrical power output. The load test analysis of the KAWECS emulator system shows the performance of the proposed PMSM-based emulator for varying load demands with the speed and torque reference values from the kite model.

We simulated three different power ratings, 1 kW, 10 kW, and 100 kW, with the resultant aerodynamic coefficient C_R of 1.125, 2.875, and 3.825, respectively, at the generator terminal shown in Figure 14. The kite's area depends on the airfoil's design and the rated wind speed. The ratings of the designed KAWECS for three power ratings are shown in Table 1. Figure 14a–c show the performance of the 1 kW, 10 kW, and 100 kW emulator system, respectively. The analysis of various power ratings shows that the KAWECS emulator can be used to test the scaled-up version of the system under varying load conditions, which is crucial in analysing the performance of KAWECS prior to the development of the actual system.

3.3. Field Test Data Analysis

The kite flight data collected from the field test was used to estimate the force. The tether force along with the kite's figure-of-eight trajectory data were recorded through several experiments. The raw data from the field testing are shown in Table 3 and include the kite orientation information (yaw, pitch, and roll), the kite's altitude in meters, the force measured by the load cell (analogue value), the wind speed (in m/s), and the wind direction (in degrees). The wind direction was recorded with respect to the east-direction axis.

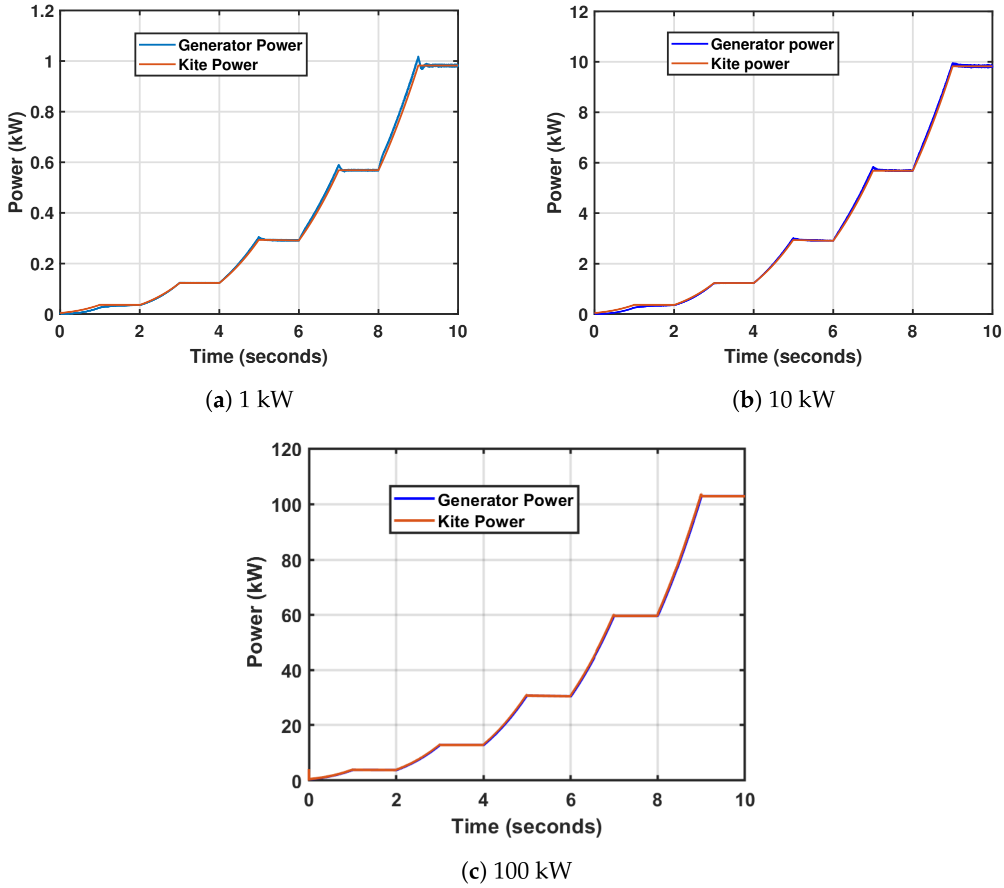

Figure 14. Electrical power output at the generator terminal of three different test cases: (**a**) 1 kW; (**b**) 10 kW; and (**c**) 100 kW.

Table 3. Field test data used in the simulation: sample data of 10 data points.

Data Point	Yaw (Degrees)	Pitch (Degrees)	Roll (Degrees)	Altitude (m)	Tether Force (N)	Wind Speed (m/s)	Wind Direction (Degrees)
1	50.68	−131.76	48.03	1.90	481	3.58	17
2	48.37	−135.88	52.03	2.40	485	3.53	14
3	45.94	−143.90	54.68	4.90	453	3.55	9
4	47.20	−147.42	54.78	5.90	464	3.60	8
5	48.21	−149.27	46.20	7.10	467	3.60	11
6	52.36	−151.14	35.22	8.10	450	3.63	13
7	54.88	−155.88	29.09	10.20	372	3.63	6
8	56.07	−156.77	25.46	10.60	283	3.68	6
9	54.80	−160.40	25.39	12.20	255	3.70	15
10	53.56	−166.97	27.68	13.80	211	3.65	12

We may write the C_L and C_D equations as

$$C_L \approx 2\pi(\dot{\theta} - \beta) \tag{34}$$

$$C_D \approx 1.28 \cdot (sin(\dot{\theta}) + cos(\beta) + cos(\phi')) \tag{35}$$

where β is the angle made by the kite with respect to the wind direction vector and is calculated as $|\chi - \psi|$ [42]. The χ is the angle made by the wind direction vector with respect to the east-direction vector and ψ is the angle made by the kite with respect to the east-direction vector.

Figure 15 depicts the kite's flight path in the experimental field. As the kite moved in a figure-of-eight trajectory, the force changed according to the position. The kite trajectory was plotted using the GPS data received during the field test. Figure 15a depicts the yaw vs. force, Figure 15b shows the roll vs. force, and Figure 15c shows the pitch vs. force, which shows the corresponding YRP angles during the kite's trajectory.

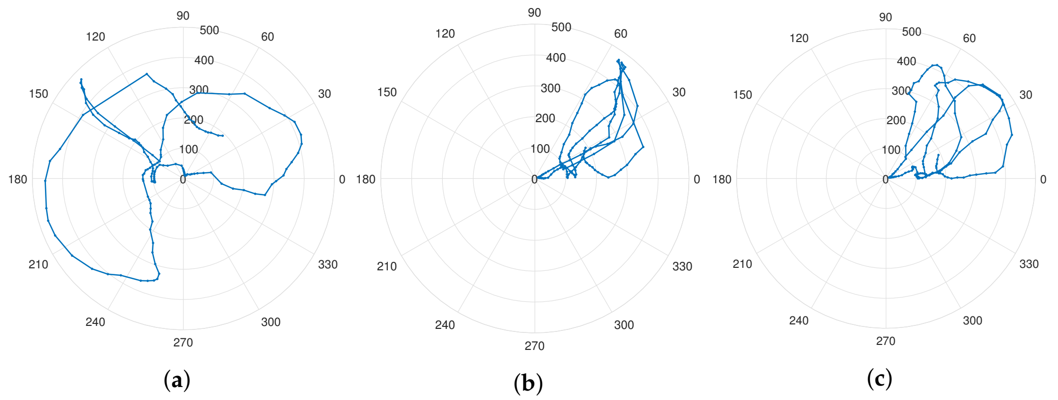

Figure 15. Polar plot of kite flight path test: (**a**) yaw vs. force; (**b**) roll vs. force; (**c**) pitch vs. force. Adopted from [42].

3.4. Simulation Using the Satellite Data

The pictorial representation of the satellite-derived wind data is shown in Figures 16 and 17 for the National Institute of Technology Karnataka (NITK) beach location at a height of 10 m and 50 m, respectively. NITK is situated in the Dakshina Kannada district of Karnataka state in India. The aforementioned satellite wind analysis is shown for two levels of height: 10 m and 50 m. Figures 16a and 17a show the wind speed and direction for 12 months of the year 2022 at 17:00 IST, whereas Figures 16b and 17b represent the wind speed and direction for 24 h from the month of August's wind profile. Finally, we obtained most of the wind speed and direction variation from the plot towards the south-east direction, and the wind speed varies from 2 m/s to 8 m/s.

Figure 18 shows the power generation plot from hourly satellite wind data at a 50 m height from the ground and takes 50 wind data samples in the month of August, which was simulated in the KAWECS model and is shown in simulation results below. Figure 18a shows the wind speed variations from 2.75 m/s to 6 m/s. Figure 18b shows the motor speed in rpm, which varies from 325 rpm to 730 rpm. Figure 18c shows the kite power in watts, which varies from 95 W to 830 W, and Figure 18d shows the generator power in watts, which changes from 95 W to 820 W and matches exactly with the kite generated power. Figure 19 shows the power generation plot from hourly satellite wind data at a 50 m height from the ground.

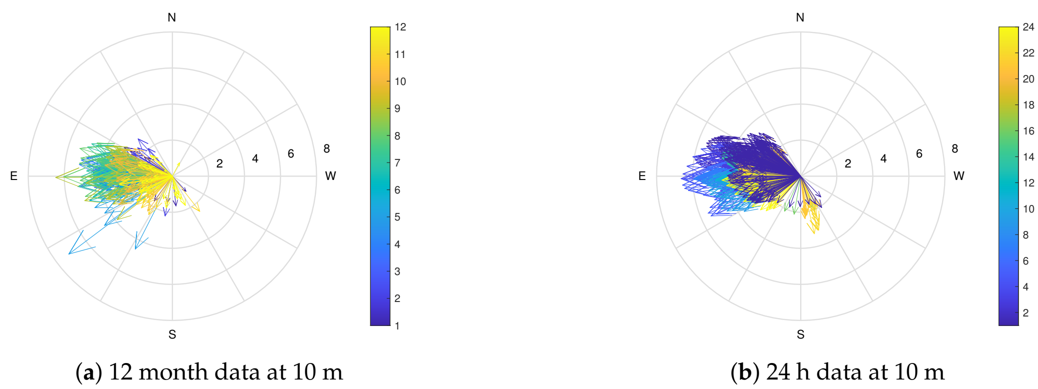

Figure 16. Wind data from satellite: plot (**a**) shows the wind profile for 12 months at 17:00 IST, at a 10 m height, and plot (**b**) shows 24 h of wind profile for the month of August, at a 10 m height.

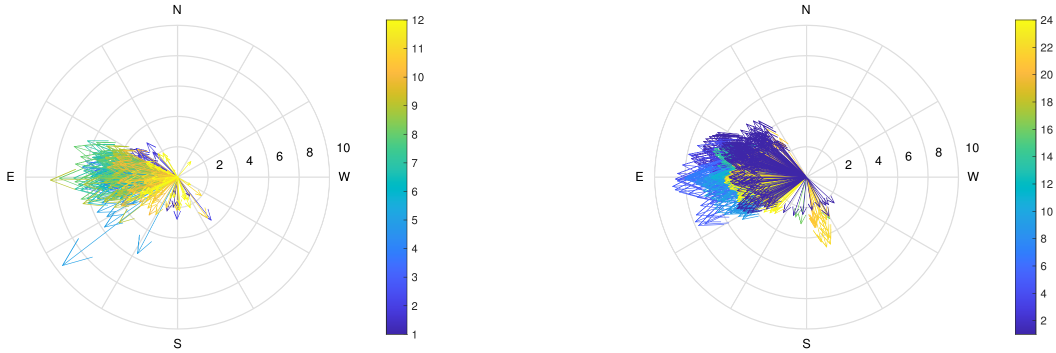

(**a**) 12 month data at 50 m (**b**) 24 h data at 50 m

Figure 17. Wind data from satellite: plot (**a**) shows the wind profile for 12 months at 17:00 IST, at a 50 m height, and plot (**b**) shows 24 h of wind profile for the month of August, at a 50 m height.

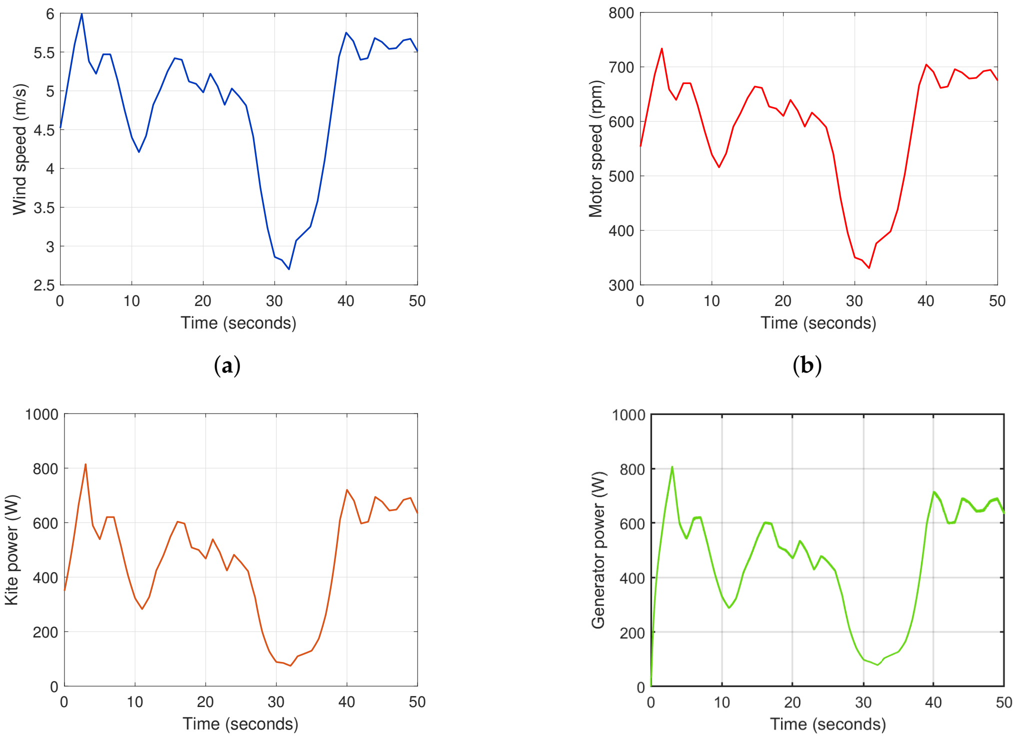

(**a**) (**b**) (**c**) (**d**)

Figure 18. Plots using hourly satellite wind data at a 50 m height from the ground: (**a**) wind speed; (**b**) motor speed; (**c**) estimated kite power from physical model; and (**d**) generator electrical power.

From the satellite data, 50 wind data samples in the month of August were simulated in the KAWECS model and are shown in the simulation results. Figure 19a shows the wind speed in m/s, which varies from 1.9 m/s to 4.75 m/s. Figure 19b shows the motor speed in rpm, which varies from 230 rpm to 582 rpm. Figure 19c shows the kite power in watts, which varies from 34 W to 392 W, and Figure 19d shows the generator power in watts, which changes from 34 W to 392 W and matches exactly with kite generated power.

3.5. Verification Using Experimental Data

Figure 20 shows the ground data simulation results of the motor speed, the measured kite power from a field test, the estimated kite power from a physical model, the coupling/mechanical power, and the generator electrical power. The recorded data from the field testing was used to estimate the power. Data from the kite's figure-of-eight trajectory were recorded alongside the wind velocity and tether force in a series of experiments.

Figure 20a depicted the experimental wind speed, with a minimum change of 3.15 m/s and a maximum change of 4.65 m/s.

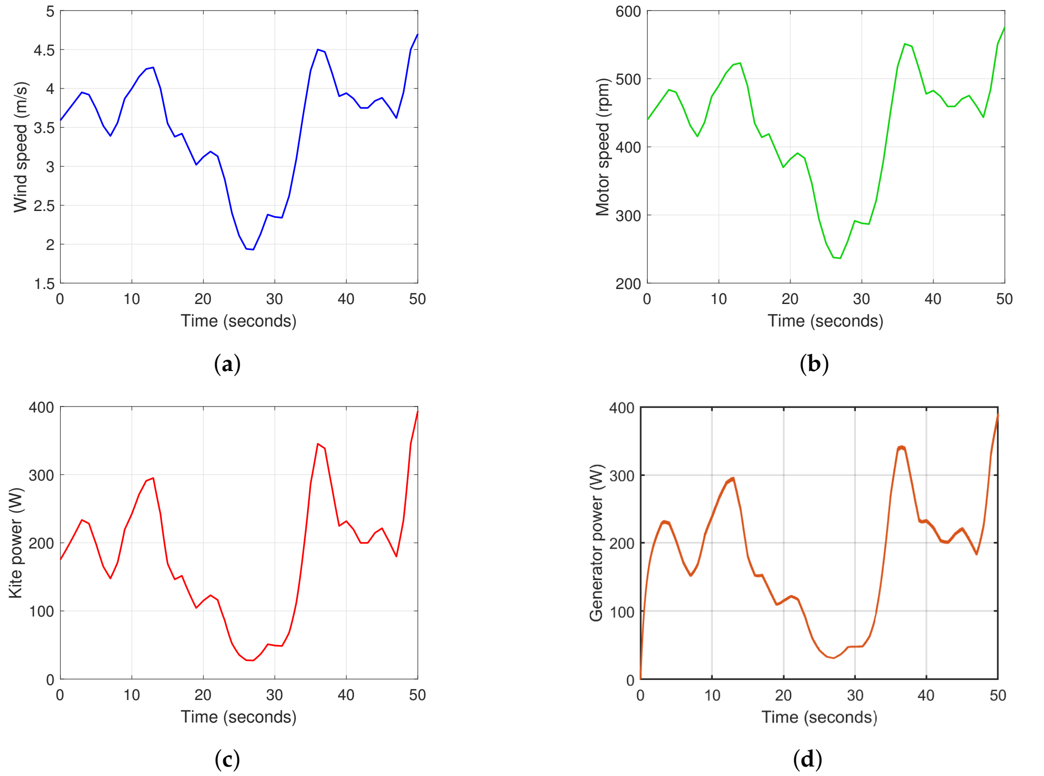

Figure 19. Power generation plot from hourly satellite wind data at a 10 m height from the ground: (**a**) wind speed; (**b**) motor speed; (**c**) estimated kite power from physical model (PM); and (**d**) generator electrical power.

Figure 20b shows the motor reference speed with a 1:5 gear ratio, with a minimum value of 387.255 rpm and a maximum value of 570 rpm. Figure 20c shows the measured kite power from the field test, which varies with a minimum value of 174.48 W and a maximum value of 674.68 W at sample times of 36 and 26 s, respectively. Figure 20d shows the estimated kite power from the physical model, which varies with a minimum value of 100 W and a maximum value of 675 W at sample times of 13 and 24 s, respectively. Figure 20e shows the coupling or mechanical power of the permanent magnet of synchronous machines, which varies with a minimum value of 100 W and a maximum value of 690 W at sample times of 13 and 24 s, respectively. Figure 20f shows the emulator electrical power at the permanent magnet synchronous generator terminal or resistive load terminal, which changes with a minimum value of 100 W and a maximum value of 675 W at sample times of 13 and 24 s, respectively. This is precisely the same as the estimated kite power from the physical model.

3.6. Discussion and Applications

The results of the study discussed in this paper contain crucial outcomes for the emulation of kite-based power generators for scaling up the system. The PMSM-based drive provides the required response to the variables provided by the kite model. For a power range of 100 kW, a 60 m^2 kite is necessary, with a resultant aerodynamic coefficient of 3.825. As the kite-based wind power generation system has a variable speed and variable frequency output at the generator, the PMSM is preferred over DC generators and induction generators [43]. A three-phase PMSG was used in this analysis, which can be driven with the required speed and torque characteristics for the kite model using the feedback loops. As a stand-alone application, a PMSM is preferred over other AC generators [44] as the field is produced by the permanent magnets, which do not need an external source to excite the machine [45]. The variations in the wind speeds were generated by three methods in this simulation: using a signal builder, using satellite data of the site, and using experimental data from the field tests. The potential application of this technology is as a stand-alone power generation unit in a region where conventional wind turbines are not practical. Kite-based power generators can be installed in remote locations where the utility grid is not available [46]. The kite power system in combination with battery storage system [47] can also be employed in remote locations where an uninterrupted power supply is necessary [48,49]. From the simulated graphs, we can understand the dynamics of the system for a specific wind profile and a kite-based system can be designed based on the requirements.

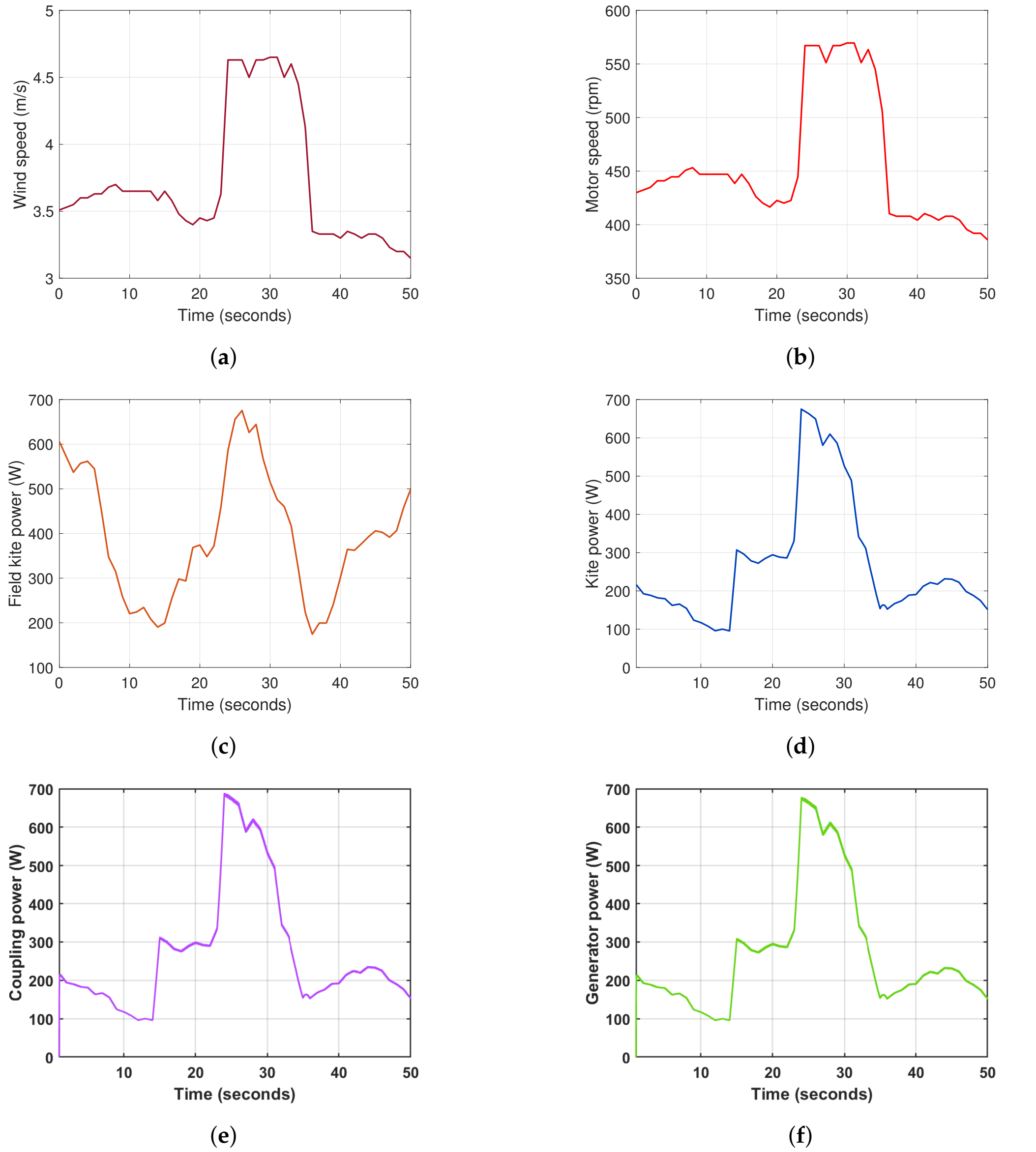

Figure 20. Simulation using experimental data: (**a**) wind speed; (**b**) motor speed; (**c**) measured kite power from a field test; (**d**) estimated kite power from the physical model; (**e**) coupling/mechanical power; and (**f**) generator electrical power.

4. Conclusions

The research described in this paper contributes to the study of power emulation in a commercial-scale Kite-based Airborne Wind Energy Conversion System (KAWECS). A KAWECS emulator was designed and simulated to mimic an actual KAWECS drive train in a controlled testing environment. In this paper, we studied the KAWECS emulator with PMSM, driven by a Field Orientation Control (FOC) technique. A three-phase power inverter drove the PMSM with a PI current controller operating in a closed loop. We validated the emulator results with the experimental field test data of the kite. The key outcomes of this research are listed below:

- The KAWECS emulator based on an FOC-controlled PMSM offers precise control over speed and torque, which can mimic the kite characteristics accurately;
- The KAWECS emulator offers a wide range of kite sizes at varying wind speeds, which can help researchers to realise the system prior to implementation to study the dynamics of the system;
- The proposed KAWECS emulator was simulated with three power ranges of 1 kW, 10 kW, and 100 kW at a kite surface area of 2.5 m^2, 14 m^2, and 60 m^2, respectively, at the generator terminal;
- The wind speed varied from 2 m/s to 12.25 m/s for both no-load and full-load rated conditions. We used experimental ground test data to verify the system and the dynamic behaviour of the generator under no-load and on-load conditions;
- The hourly satellite wind speed data at 10 m and 50 m above the ground was considered in this study with the figure-of-eight data from the field tests to emulate the power generation from KAWECS. The wind speed data at a 50 m height with a maximum power of 820 W was generated with a kite area of 10 m^2 at a maximum wind speed of 6 m/s. The wind speed data at the height of 10 m with a maximum power of 392 W was generated with a kite area of 10 m^2 at a maximum wind speed of 4.65 m/s;
- The comparative study of the KAWECS and CWT at a 2 MW power range showed that the capacity factor of the KAWECS is 45.59% compared to 31.36% for the CWT, indicating a 45% increased average power production in the KAWECS, which is one of the highest factors in the wind energy industry.

The analysis shows that the kite power derived from the mathematical model satisfies the generated power from the emulation system. The kite's tether force varies throughout the kite's flight trajectory, which needs precise control of the generator shaft speed. The PMSM-based emulator system offers promising results for emulating a KAWECS with various sizes of kites and varying wind profiles. The cut-out speed is a critical factor in a wind energy conversion system and in a KAWECS, and the kite steering unit was used to lower the elevation angles to depower and land the kite. The integration of kite steering unit with the power emulator will be the future scope of this study. The research work described in this paper is a step forward in exploiting KAWECS, making them equally efficient for use with wind turbines.

Author Contributions: Conceptualization, R.V.C.; Data curation, R.V.C.; Formal analysis, P.K. (Pankaj Kumar) and Y.K.; Funding acquisition, P.K. (Panagiotis Kosmopoulos); Investigation, P.K. (Pankaj Kumar), Y.K., A.K., M.S.K. and D.K.; Methodology, R.V.C., P.K. (Pankaj Kumar) and Y.K.; Project administration, A.K., M.S.K. and D.K.; Supervision, Y.K.; Visualization, P.K. (Panagiotis Kosmopoulos); Writing—original draft, R.V.C.; Writing—review & editing, P.K. (Pankaj Kumar) and P.K. (Panagiotis Kosmopoulos). All authors have read and agreed to the published version of the manuscript.

Funding: This research was funded by the Science and Engineering Research Board (SERB) of India under the core research grant (CRG). Fund grant number CRG/2021/007655.

Data Availability Statement: Not applicable.

Acknowledgments: The authors would like to thank the Science and Engineering Research Board (SERB) for funding the project through the core research grant (CRG). Panagiotis Kosmopoulos acknowledges the ClimSA Programme which is an initiative funded by the European Union and implemented by the Organisation of African, Caribbean and Pacific States (OACPS).

Conflicts of Interest: The authors declare no conflicts of interest.

References

1. Olabi, A.G.; Wilberforce, T.; Elsaid, K.; Sayed, E.T.; Salameh, T.; Abdelkareem, M.A.; Baroutaji, A. A review on failure modes of wind turbine components. *Energies* **2021**, *14*, 5241. [CrossRef]
2. Saleem, A.; Kim, M.H. Aerodynamic analysis of an airborne wind turbine with three different aerofoil-based buoyant shells using steady RANS simulations. *Energy Convers. Manag.* **2018**, *177*, 233–248. [CrossRef]
3. Ghosh, A.; Biswas, A.; Sharma, K.; Gupta, R. Computational analysis of flow physics of a combined three bladed Darrieus Savonius wind rotor. *J. Energy Inst.* **2015**, *88*, 425–437. [CrossRef]
4. Ackermann, T.; Söder, L. Wind energy technology and current status: A review. *Renew. Sustain. Energy Rev.* **2000**, *4*, 315–374. [CrossRef]
5. Kolar, J.W.; Friedli, T.; Krismer, F.; Looser, A.; Schweizer, M.; Friedemann, R.A.; Steimer, P.K.; Bevirt, J.B. Conceptualization and multiobjective optimization of the electric system of an airborne wind turbine. *IEEE J. Emerg. Sel. Top. Power Electron.* **2013**, *1*, 73–103. [CrossRef]
6. Peçanha, L.B.C.; Oliveira, N.d.S.B.; Bretas, W.V. Generation of Wind Energy with Kites: A Review of the Airborne Wind Energy Technology. In Proceedings of the 2020 IEEE PES Transmission & Distribution Conference and Exhibition-Latin America (T&D LA), Montevideo, Uruguay, 28 September–2 October 2020; IEEE: Piscataway, NJ, USA, 2020; pp. 1–6.
7. Loyd, M. crosswind kite power for large-scale wind power production. *Energy* **1980**, *4*, 106–111. [CrossRef]
8. Cherubini, A.; Papini, A.; Vertechy, R.; Fontana, M. Airborne Wind Energy Systems: A review of the technologies. *Renew. Sustain. Energy Rev.* **2015**, *51*, 1461–1476. [CrossRef]
9. Zillmann, U.; Bechtle, P. Emergence and economic dimension of airborne wind energy. In *Airborne Wind Energy: Advances in Technology Development and Research*; Springer: Berlin/Heidelberg, Germany, 2018; pp. 1–25.
10. Fagiano, L.; Nguyen-Van, E.; Rager, F.; Schnez, S.; Ohler, C. Autonomous takeoff and flight of a tethered aircraft for airborne wind energy. *IEEE Trans. Control Syst. Technol.* **2017**, *26*, 151–166. [CrossRef]
11. De Lellis, M.; Mendonça, A.; Saraiva, R.; Trofino, A.; Lezana, A. Electric power generation in wind farms with pumping kites: An economical analysis. *Renew. Energy* **2016**, *86*, 163–172. [CrossRef]
12. Salari, M.E.; Coleman, J.; Toal, D. Airborne Wind Energy—A Review. In Proceedings of the 3rd International Congress on Energy Efficiency and Energy Related Materials (ENEFM2015), Oludeniz, Turkey, 19–23 October 2015; Springer: Berlin/Heidelberg, Germany, 2015; p. 81.
13. Bechtle, P.; Schelbergen, M.; Schmehl, R.; Zillmann, U.; Watson, S. Airborne wind energy resource analysis. *Renew. Energy* **2019**, *141*, 1103–1116. [CrossRef]
14. Masters, G.M. *Renewable and Efficient Electric Power Systems*; John Wiley and Sons: Hoboken, NJ, USA, 2013.
15. Costello, S.; Franois, G.; Bonvin, D. Crosswind kite control–a benchmark problem for advanced control and dynamic optimization. *Eur. J. Control* **2017**, *35*, 1–10. [CrossRef]
16. Costello, S.; François, G.; Bonvin, D. Real-time optimizing control of an experimental crosswind power kite. *IEEE Trans. Control Syst. Technol.* **2017**, *26*, 507–522. [CrossRef]
17. Ahmed, M.S.; Hably, A.; Bacha, S. Kite generator system modeling and grid integration. *IEEE Trans. Sustain. Energy* **2013**, *4*, 968–976. [CrossRef]
18. Erhard, M.; Strauch, H. Flight control of tethered kites in autonomous pumping cycles for airborne wind energy. *Control Eng. Pract.* **2015**, *40*, 13–26. [CrossRef]
19. Todeschini, D.; Fagiano, L.; Micheli, C.; Cattano, A. Control of a rigid wing pumping airborne wind energy system in all operational phases. *Control Eng. Pract.* **2021**, *111*, 104794. [CrossRef]
20. Ali, Q.S.; Kim, M.H. Power conversion performance of airborne wind turbine under unsteady loads. *Renew. Sustain. Energy Rev.* **2022**, *153*, 111798. [CrossRef]
21. Salari, M.E.; Coleman, J.; O'Donnell, C.; Toal, D. Experimental rig investigation of a direct interconnection technique for airborne wind energy systems. *Int. J. Electr. Power Energy Syst.* **2020**, *123*, 106300. [CrossRef]
22. Licitra, G.; Koenemann, J.; Bürger, A.; Williams, P.; Ruiterkamp, R.; Diehl, M. Performance assessment of a rigid wing Airborne Wind Energy pumping system. *Energy* **2019**, *173*, 569–585. [CrossRef]
23. Coleman, J.; Ahmad, H.; Pican, E.; Toal, D. Non-reversing generators in a novel design for pumping mode airbornewind energy farm. In *Airborne Wind Energy*; Springer: Berlin/Heidelberg, Germany, 2013; pp. 587–597.
24. Ahmed, M.; Hably, A.; Bacha, S.; Ovalle, A. Kite generator system: Grid integration and validation. In Proceedings of the IECON 2014-40th Annual Conference of the IEEE Industrial Electronics Society, Dallas, TX, USA, 29 October–1 November 2014; IEEE: Piscataway, NJ, USA, 2014; pp. 2139–2145.
25. Martinez, F.; Herrero, L.C.; de Pablo, S. Open loop wind turbine emulator. *Renew. Energy* **2014**, *63*, 212–221. [CrossRef]
26. Singla, M.K.; Gupta, J.; Nijhawan, P.; Ganguli, S.; Rajest, S.S. Development of an Efficient, Cheap, and Flexible IoT-Based Wind Turbine Emulator. In *Business Intelligence for Enterprise Internet of Things*; Springer International Publishing: Berlin/Heidelberg, Germany, 2020; pp. 225–231.
27. Battaiotto, P.; Mantz, R.; Puleston, P. A wind turbine emulator based on a dual DSP processor system. *Control Eng. Pract.* **1996**, *4*, 1261–1266. [CrossRef]

28. Bagaber, B.; Junge, P.; Mertens, A. Lifetime Estimation and Dimensioning of the Machine-Side Converter for Pumping-Cycle Airborne Wind Energy System. In Proceedings of the 2020 22nd European Conference on Power Electronics and Applications (EPE'20 ECCE Europe), Lyon, France, 7–11 September 2020; IEEE: Piscataway, NJ, USA, 2020; p. 1.
29. Saberi, S.; Rezaie, B. Robust adaptive direct speed control of PMSG-based airborne wind energy system using FCS-MPC method. *ISA Trans.* **2022**, *131*, 43–60. [CrossRef] [PubMed]
30. von den Hoff, D.; Haberschusz, D.; Rotering, N.; De Doncker, R. Design and Evaluation of a Battery-Supported Electric Drivetrain for Kite-Based High-Altitude Wind Energy Conversion. In Proceedings of the 2019 Conference for Wind Power Drives (CWD), Aachen, Germany, 12–13 March 2019; IEEE: Piscataway, NJ, USA, 2019; pp. 1–10.
31. Bauer, F.; Hackl, C.M.; Smedley, K.; Kennel, R.M. "Virtual"-power-hardware-in-the-loop simulations for crosswind kite power with ground generation. In Proceedings of the 2016 American Control Conference (ACC), Boston, MA, USA, 6–8 July 2016; IEEE: Piscataway, NJ, USA, 2016; pp. 4071–4076.
32. Bagaber, B.; Mertens, A. A Parallel Voltage Source Converter and Diode Rectifier PMSM Drive Concept for Decoupling the Thermal Cycles in the Machine-Side Converter of an Airborne Wind Energy Generator. In Proceedings of the 2021 23rd European Conference on Power Electronics and Applications (EPE'21 ECCE Europe), Virtually, 6–10 September 2021; IEEE: Piscataway, NJ, USA, 2021; p. 1.
33. Bagaber, B.; Heide, D.; Ponick, B.; Mertens, A. Efficiency and Lifetime Analysis of Several Airborne Wind Energy Electrical Drive Concepts. In Proceedings of the 2022 24th European Conference on Power Electronics and Applications (EPE'22 ECCE Europe), Hanover, Germany, 5–9 September 2022; IEEE: Piscataway, NJ, USA, 2022; pp. 1–11.
34. van der Vlugt, R.; Bley, A.; Noom, M.; Schmehl, R. Quasi-steady model of a pumping kite power system. *Renew. Energy* **2019**, *131*, 83–99. [CrossRef]
35. Schmehl, R.; Noom, M.; van der Vlugt, R. Traction power generation with tethered wings. In *Airborne Wind Energy*; Springer: Berlin/Heidelberg, Germany, 2013; pp. 23–45.
36. Noom, M. Theoretical Analysis of Mechanical Power Generation by Pumping Cycle Kite Power Systems. Master's Thesis, TU Delft, Delft, The Netherlands, 2013.
37. Fechner, U.; Schmehl, R. Feed-forward control of kite power systems. *J. Phys. Conf. Ser.* **2014**, *524*, 012081. [CrossRef]
38. Ba, X.; Gong, Z.; Guo, Y.; Zhang, C.; Zhu, J. Development of equivalent circuit models of permanent magnet synchronous motors considering core loss. *Energies* **2022**, *15*, 1995. [CrossRef]
39. Suman, K.; Mathew, A.T. Speed control of permanent magnet synchronous motor drive system using PI, PID, SMC and SMC plus PID controller. In Proceedings of the 2018 International Conference on Advances in Computing, Communications and Informatics (ICACCI), Bangalore, India, 19–22 September 2018; IEEE: Piscataway, NJ, USA, 2018; pp. 543–549.
40. Kim, K.H.; Van, T.L.; Lee, D.C.; Song, S.H.; Kim, E.H. Maximum output power tracking control in variable-speed wind turbine systems considering rotor inertial power. *IEEE Trans. Ind. Electron.* **2012**, *60*, 3207–3217. [CrossRef]
41. Yan, J.; Lin, H.; Feng, Y.; Guo, X.; Huang, Y.; Zhu, Z. Improved sliding mode model reference adaptive system speed observer for fuzzy control of direct-drive permanent magnet synchronous generator wind power generation system. *IET Renew. Power Gener.* **2013**, *7*, 28–35. [CrossRef]
42. Castelino, R.V.; Kashyap, Y.; Kosmopoulos, P. Airborne Kite Tether Force Estimation and Experimental Validation Using Analytical and Machine Learning Models for Coastal Regions. *Remote Sens.* **2022**, *14*, 6111. [CrossRef]
43. Bansal, R.; Bhatti, T.; Kothari, D. On some of the design aspects of wind energy conversion systems. *Energy Convers. Manag.* **2002**, *43*, 2175–2187. [CrossRef]
44. Spooner, E.; Williamson, A. Direct coupled, permanent magnet generators for wind turbine applications. *IEE Proc.-Electr. Power Appl.* **1996**, *143*, 1–8. [CrossRef]
45. Pereira, A.F.; Sousa, J.M. A Review on Crosswind Airborne Wind Energy Systems: Key Factors for a Design Choice. *Energies* **2022**, *16*, 351. [CrossRef]
46. Reuchlin, S.; Joshi, R.; Schmehl, R. Sizing of Hybrid Power Systems for Off-Grid Applications Using Airborne Wind Energy. *Energies* **2023**, *16*, 4036. [CrossRef]
47. Mittal, R.; Sandhu, K.; Jain, D. Battery energy storage system for variable speed driven PMSG for wind energy conversion system. In Proceedings of the 2010 Joint International Conference on Power Electronics, Drives and Energy Systems & 2010 Power India, New Delhi, India, 20–23 December 2010; IEEE: Piscataway, NJ, USA, 2010; pp. 1–5.
48. Ilyushin, Y.V.; Afanaseva, O.V. Development of scada-model for trunk gas pipeline's compressor station. *J. Min. Inst.* **2019**, *240*, 686–693. [CrossRef]
49. Afanaseva, O.; Ilyushin, Y. Analysis and synthesis of distributed icedrill heating control system of mountain reconnaissance drilling rig. *Int. Multidiscip. Sci. Geoconf. SGEM* **2018**, *18*, 41–47.